

Effects of Different Pore Structures on Loading and Sustained-Release of MMC by Hollow Mesoporous Fe(0)@mSiO₂

Ziling Chang

East China University of Science and Technology

Mengyang Dong

East China University of Science and Technology

Huafei Li

Shanghai University

Yuxiang Yang (✉ yxyang@ecust.edu.cn)

East China University of Science and Technology

Hongming Yuan

Jilin University

Chaoying Ni

University of Delaware

Research Article

Keywords: hollow magnetic nano-spheres, particle size, mitomycin C, sustained-release, targeting label

Posted Date: April 8th, 2022

DOI: <https://doi.org/10.21203/rs.3.rs-1500266/v1>

License: © ⓘ This work is licensed under a Creative Commons Attribution 4.0 International License.

[Read Full License](#)

1 Si-C₁₆-MMC composites follows pseudo-first-order attributable to its special pore
2 structure. For this reason the inner cavity of HMFe-Si-C₁₆ could be labeled with
3 radioisotope ⁹⁹Tc^m to study the magnetic targeting distribution of HMFe-Si-C₁₆ in
4 vivo, and its cytotoxicity against in vitro HeLa cells was also studied. These results
5 indicate the potential of HMFe-Si-C₁₆ in the magnetic targeted drug delivery system.

6 **Keywords:** hollow magnetic nano-spheres · particle size · mitomycin C · sustained-
7 release · targeting label

8

9 1. Introduction

10 MMC is a class of antibiotics for cancer whose chemical structure has three
11 active groups of quinone, acetyl imide and ammonium carbamate. Its action is similar
12 to that of an alkylating agent, forming cross-linking with the DNA chain and
13 inhibiting DNA replication. MMC has an obvious antitumor effect, but its side effects
14 are serious [1-3]. Delivery through the carrier can increase the potency of the drug
15 and reduce side effects. Many studies have used magnetic nanomaterials loaded with
16 MMC to achieve targeted drug delivery. Zhu et al. [4] synthesized magnetic
17 nanoparticles with albumin as the carrier material, though the MMC loading was only
18 6%. M. Eizadi Sharifabad et al. [5] carried out the coprecipitation method and
19 following self-assembled lipid tubules as templates to obtain liposome silicon coated
20 10 nm magnetic core, while the highest MMC loading only reached at 7μg/mg. Li et
21 al. [6] synthesized mPEG-PLA diblock copolymer conjugate by ring-opening
22 polymerization of l-lactide using stannous acid as a catalysis, the drug loading in
23 micelles of copolymer conjugate ranged from 11.23% to 20.01%. It seems the
24 copolymer conjugate is promising material to load MMC, though there still exists
25 some drawbacks, such as complex synthesis and multiple fabrication process, as well
26 as low load of MMC.

27 At present, mesoporous silica (mSiO₂) nanoparticles with high surface area, large

1 pore volume, uniform pore size and high biocompatibility become attractive as drug
2 delivery carriers[7-9]. However, mesoporous silica as a drug carrier has some
3 limitations, such as the inability to deliver drugs directly to organ and site specific
4 tumors, and it ineffectively being used for regional target therapy, especially since
5 anticancer drugs have the ability to damage normal cells [10-12]. In order to promote
6 therapeutic efficiency and avoid damage caused by drug toxicity in normal cells, the
7 integration of mesoporous silica with nano-magnetic materials can indeed achieve this
8 goal by introducing drugs into tumor target cells. It is expected that the specific
9 surface area will increase significantly when mesoporous silica is coated onto the
10 surface of the metal nanoparticles (NPs), which may provide an abundant capacity to
11 load drug molecules[13].

12 By using metal NPs as core material, metal NPs@mSiO₂ with a uniform size will
13 be readily prepared. In addition, the metal NPs core can impart mSiO₂ with unique
14 physicochemical properties, such as large remanence, low cytotoxicity and higher
15 magnetism compared with traditional mesoporous materials, which can pave the way
16 to more advanced applications [14,15]. Ohhashi et al. [16] fabricated Au nanoparticle
17 (NP)@mSiO₂@metal-organic framework (MOF) via a modified Stober method based
18 on the hydrolysis-condensation mechanism and selective nucleation and growth. The
19 obtained triple-compartment hybrids can be employed in sensing materials on the
20 basis of the fluorescence properties of the doped fluorescent molecules within the
21 mSiO₂ phase and show plasmonic properties due to the Au NPs.

22 So far, mesoporous hollow spheres using Fe(0) NPs as core coated with are
23 rarely reported. Mengmeng Song et al. [13] fabricated core-shell structured
24 Fe@mSiO₂ nanowires for targeted drug delivery have been prepared through
25 electrodeposition followed by a CTAB-template sol-gel process. Due to the large

1 surface area of the mesoporous silica shell, Fe@mSiO₂ nanowires have a good
2 capability for loading drug molecules, MTT results and LDH assay demonstrated
3 Fe@mSiO₂ as a potential application as a drug nanocarrier for magnetic-targeted drug
4 delivery. Tingting Liu [17] demonstrated Fe@mSiO₂ had the potential to be used for
5 targeted drug delivery.

6 Here, we will report a new method to fabricate HMFe-Si by trapping core-shell
7 Fe(0)@SiO₂ nanoparticles into mesoporous silica with surfactant
8 octadecyltrimethoxysilane (C₁₈TMS) acting both as a template and silica source
9 according to previous work [18]. The most obvious advantage of the dual-function
10 template method is its ability to avoid the formation of a non-uniform mesoporous
11 silica shell and obtain uniformly size-distributed magnetic nanoparticles with high
12 saturation magnetization value. However, drug carriers with a diameter of ~100 nm
13 are more effective for chemotherapy and gene delivery [19] —they are capable of
14 penetrating the blood–brain barrier and the blood-testis barrier, have rapid distribution
15 to the body, while also not affecting the function of organs.

16 So we propose our query, whether to adjust the chain length of dual-function
17 template to obtain HMFe-Si with diameter approaching ~100 nm and high saturation
18 magnetization value. Our previous work perhaps supports our idea, owing to the fact
19 that [20] the chain length is an important chemical factor: the longer facilitates the
20 formation of millimeter-scaled silica ropes, while the shorter leads to the formation of
21 micrometer-scaled rope fibers of mesoporous silica with 2D hexagonal structure.

22 The dual-function template of hexadecyltrimethoxysilane (C₁₆TMS) with shorter
23 chain length in place of surfactant octadecyltrimethoxysilane (C₁₈TMS) was used to
24 fabricate HMFe-Si with diameter approaching ~100 nm. As a consequence of the
25 large hollow cavity space and high saturation magnetization value, we also performed

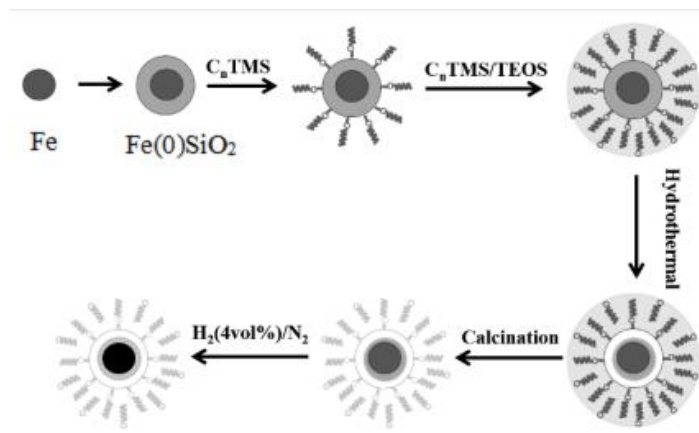
1 MMC loading and releasing on MMC-loaded HMFe-Si, as well as $^{99}\text{Tc}^{\text{m}}$ labeled
2 HMFe-Si, to study magnetic targeting distribution in vivo.

3 2. Experimental

4 2.1. Materials

5 Iron (III) chloride hexahydrate, hydrochloric acid, iso-Propyl alcohol, ammonium
6 hydroxide, tetraethyl orthosilicate, and ethanol (all of analytical grade) were
7 purchased from Shanghai Sinopharm Chemical Reagent Co., Ltd. (Shanghai, China).
8 Hexadecyltrimethoxysilane and octadecyltrimethoxysilane were purchased from
9 Aladdin industrial Corporation (Shanghai, China). Mitomycin C was purchased from
10 Hubei Honch Pharmaceutical Co., Ltd. Pertechnetate ($^{99}\text{Tc}^{\text{m}}$) Sodium injection was
11 purchased from Shanghai Atom Kexing Pharmaceutical Co., Ltd.

12 2.2. Synthesis strategy and formation mechanism of the approach



13

14 Fig. 1. Scheme of the synthetic procedure of HMFe-Si (Fe(0)@SiO₂@C_nTMS)

15 The hollow magnetic nano-spheres can be obtained by using either sacrificial
16 templates in the core area or selective etching inner layer of silica [21], the surfactant
17 C_nTMS here is a dual-function agent for both the stabilization of hematite core and
18 mesoporous directing template, and the resulted structure can be either strict
19 hematite/MSN core/shell or hematite embedded in MSN framework in a scattered
20 manner. An assembly route to synthesize of HMFe-Si can be described as shown in

1 Fig. 1.

2 First, the silica is closely coated on the core of hematite (Fe(0)), the active
3 trimethoxysilane of the part surfactant C_n TMS then reacts with hydroxyl groups of the
4 silica surface coated on the hematite core to form hydrophobic micellar-type of the
5 clusters around Fe(0)@SiO₂. Third, hydrophobic alkyl chains part of (C₁₆-C₁₈ alkyl)
6 trimethoxysilane are inserted into hydrophobic micelle according to the principle of
7 minimum energy [31], and the TEOS assembles into ordered mesoporous silica
8 directed by the C₁₆-C₁₈ alkyl chain, while active trimethoxysilane of inserted C_n TMS
9 hydrolyzes into oligomeric silica species inside the palisade layer between alkyl
10 chains, and an end capping self-assembly of mesoporous silica surround Fe(0)@SiO₂.
11 Finally, through the next process of hydrothermal, calcination and hydrogrn
12 reductions, the HMFe-Si can be obtained. From Fig. 1, it can be observed that the size
13 of HMFe-Si is based on the chain length of C_n TMS. When the C₁₈ alkyl chain is
14 replaced by C₁₆ alkyl chain, the obtained HMFe-Si certainly shows a smaller size.

15 2.3. Synthesis of Silica-Coated Magnetite Nanoparticle (Fe(0)@SiO₂)

16 Fe(0)@SiO₂ nanoparticles were prepared by aqueous phase one-pot method
17 using NaBH₄ reducing Fe³⁺, which was described as following. 100 mL of 2×10⁻⁶
18 mol/L citrate solution was deoxidized with highly purified nitrogen for 20min first,
19 then 0.08g NaBH₄ was added under mechanical stirring, with a large number of
20 bubbles appearing in the solution. As soon as 2 mL of 0.1 mol/L FeCl₃ solution was
21 added, the mixture became black immediately. Afterwards, a 400 ml of ethanol
22 solution containing 15 microliters of TEOS was quickly added and the mixture was
23 mechanically stirred for 20min at 30°C. After magnetic separation, the mixture was
24 washed three times with deionized water and absolute ethanol. Finally, the black
25 product was dried in a vacuum drying oven for 12h.

1 2.4. Preparation of Fe(0)@SiO₂@mSiO₂-C_n(n=16, 18)

2 The obtained Fe(0)@SiO₂ sample was ultrasonically dispersed in 5 mL ethanol
3 to form stock solution A, and preserved in a refrigerator at 4 °C for further use. All
4 stock solution A was added into a solution containing 2 mL of boiled deionized water,
5 10 mL of 95% ethanol, 0.72 mL of NH₃, and 0.3 mL of C₁₆TMS/TEOS mixture, with
6 the C₁₆TMS/TEOS volume ratio of 1:2.47 was then added under vigorous stirring in
7 turn at regular intervals. After reaction for 6 h at 25 °C, the Fe(0)@SiO₂@mSiO₂-C₁₆
8 were recovered by centrifugation, washed with ethanol, and dried.

9 The preparation of Fe(0)@SiO₂@mSiO₂-C₁₈ was carried out by using
10 C₁₈TMS/TEOS as substitutes for the C₁₆TMS/TEOS with the unchanged volume ratio
11 of 1:2.47, while keeping all other parameters fixed.

12 2.5. Synthesis of hollow magnetic nanoparticles (HMFe-Si-C_n)

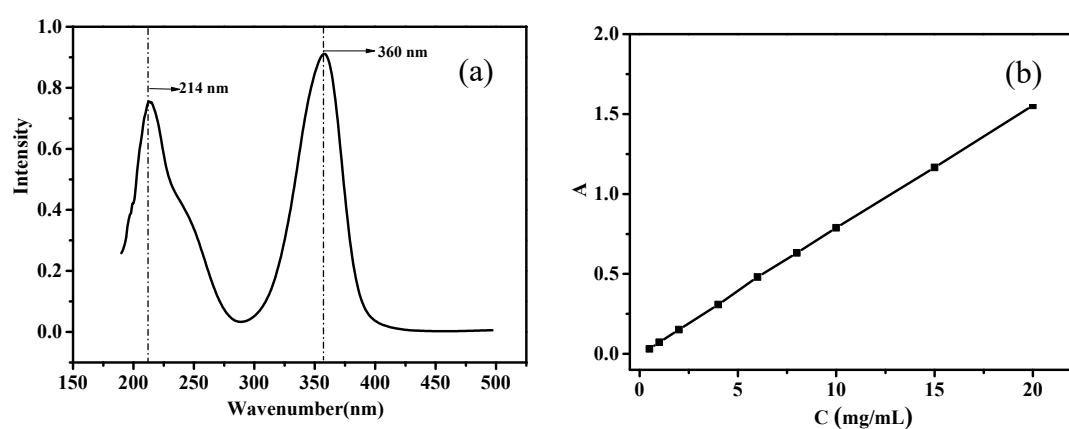
13 The hydrothermal method was employed to prepare a hollow structure, the
14 obtained Fe(0)@SiO₂@mSiO₂-C_n (n=16, 18) was dispersed in a mixture of 28 mL
15 boiled deionized water and 2 mL ethanol. The resulting solution was transferred into a
16 50 mL Teflon-lined autoclave, and the hydrothermal synthesis was carried out at
17 130 °C for 20 h. After centrifugal separating and being washed with ethanol, the
18 obtained product was vacuum dried for approximately 6 hours, and calcined in the
19 tube furnace under a nitrogen atmosphere at 550 °C for 6 h to form an outer mesopore
20 channel.

21 The hollow interior structure was obtained by selectively etching away the
22 internal homogeneous silica core of Fe(0)@SiO₂@mSiO₂-C_n. Thus the calcined
23 product was etched for 3 h in a flow of reducing H₂ (4 vol%)/N₂ gas at atmospheric
24 pressure and a temperature of approximately 400 °C. The obtained product was
25 named HMFe-Si-C_n (n=16, 18).

1 2.6. Loading and sustained-release of Mitomycin C

2 2.6.1 Standard curve of Mitomycin C

3 MMC standard stock solution of 100 $\mu\text{g}/\text{mL}$ was prepared as follows. 10.0 mg
4 MMC was ultrasonically dissolved in 50 mL of boiled deionized water, and
5 quantitatively transferred to a 100 ml volumetric flask, then be diluted to the mark
6 with boiled deionized water. Diluted MMC standard solutions of 0.5~20.0 $\mu\text{g}/\text{mL}$
7 were made by diluting 0.5~20.0 mL of MMC stock solution to 100 ml respectively.



8

9 Fig. 2. Ultraviolet absorption spectrum of MMC (a); Standard curve of the free MMC
10 concentration response to absorbance at 360 nm (b)

11 The measurement of free MMC content in the solution was carried out using
12 SHIMADZU UV-VIS Spectrophotometers UV-2600. As shown in Fig. 2a, UV-vis
13 spectrum of the MMC solution revealed two apparent broad peak wavelengths at 214
14 nm and 360 nm respectively, within ranges of 150~500 nm (Fig. 2a); the maximum
15 absorption peak was at the wavelength of 360 nm. The absorbance at 360 nm was
16 therefore used to determine the loading. The ultraviolet absorption of MMC at a
17 wavelength of 360 nm was directly proportional to the concentration of the MMC,
18 and thus the standard curve was plotted by the absorbance recorded at 360 nm versus
19 the concentration of the MMC (C, $\mu\text{g}/\text{mL}$) to determine the MMC concentration.

1 Hence, the readout at 360 nm was compared with standard curve to calculate the
2 unloaded MMC concentration. The assay mixture usually contained 0.5~20.0 µg/mL
3 MMC in boiled deionized water in a total volume of 3 mL.

4 2.6.2 MMC loading and sustained release

5 0.050 g, 0.075 g, 0.100 g, 0.150 g and 0.200 g of MMC were separately added
6 into 5 mL of n-hexane solution with 0.20 g HMFe-Si-C_n (n=16, 18), treated under
7 ultrasound for 30 min, and stirred for 12 h. The mixture within the vessel was then
8 placed in a temperature controlled shaking incubator (model: TQZ-312) at a speed of
9 150 rpm and kept at 37 °C for 24 h. Finally, the resulting MMC loaded HMFe-Si-C_n
10 was magnetically separated, followed by washing in anhydrous n-hexane, and then
11 vacuum dried at 30 °C. The supernatant liquid and washed solution were collected to
12 measure the amount of free MMC, while the MMC loaded HMFe-Si nanoparticles
13 were kept for the next release determination.

14 The MMC loading efficiency and drug loading content were calculated using the
15 following equation:

$$16 \text{ Loading efficiency} = (W_{\text{total drug}} - W_{\text{drug in supernatant}}) / W_{\text{total drug}} \times 100$$

17 The release of the MMC was carried out by distributing the above obtained
18 MMC loaded HMFe-Si-C_n in 100 mL of 10 mM phosphatebuffered saline (PBS) with
19 two different pH values (pH 5.7 and pH 7.4), which was then separated at regular
20 intervals. The released MMC concentration in 10 mM PBS was determined by
21 measuring absorbance at 360 nm and referenced to a standard curve, allowing the
22 release rate of MMC loaded HMFe-Si-C_n for MMC can be calculated.

23 2.7 Preparation of Technetium-99m (⁹⁹Tc^m) labeled hollow magnetic nano-spheres 24 (HMFe-Si-C_n) and biodistribution

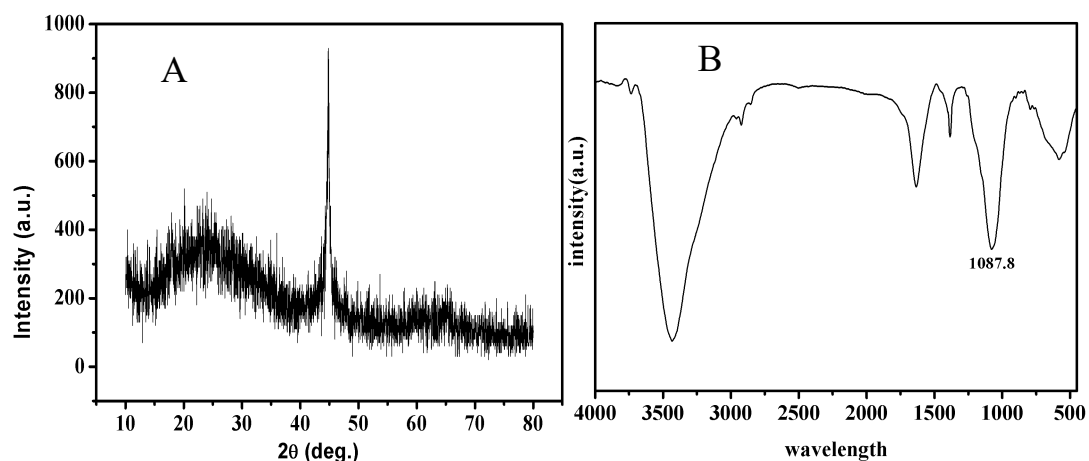
1 HMFe-Si-C_n were used for ⁹⁹Tc^m labeling in order to study the effect of these
2 encapsulation capabilities on the ⁹⁹Tc^m. The radiolabeling of HMFe-Si-C_n was carried
3 out using the reported method [22]. Briefly, 4.9 mCi of 100 μL sodium pertechnetate
4 (Na⁹⁹Tc^mO₄) was mixed with 2 mL medical saline and 400 μl stannous chloride
5 (SnCl₂) in a vial, which could reduce ⁹⁹Tc^m (VII) into ⁹⁹Tc^m (III) ions. Thereafter, 20
6 mg unlabeled HMFe-Si-C_n was poured into the reaction vial and was exposed to
7 magnetic stirring for 30 min at room temperature.

8 It was found that ⁹⁹Tc^{m3+} ions could also be adsorbed on the inner cavity and
9 outer mesopore by physical adsorption. The radiochemical purity of the labeled
10 compound was checked with a Capintec CRC-15R external dose calibrator. The
11 purified HMFe-Si-C_n-⁹⁹Tc^m was dispersed in physiological saline to generate
12 20mg/2.5mL of labeled compound solution by supersonic treatment. The results of
13 the labeling efficiency of ⁹⁹Tc^m by HMFe-Si-C_n are exhibited in Table 1.

14 To further investigate the biodistribution of HMFe-Si nanoparticles, 100μl ⁹⁹Tc^m
15 labelled HMFe-Si solution were injected into the female mice via caudal vein. After a
16 certain time in magnetically targeted therapy, the treated female mice were scanned
17 under single photoemission-computed tomography (SPECT) imaging. The animals
18 were then sacrificed with an overdose of sodium pentobarbital; following the main
19 organs (the blood, heart, lung, liver, spleen, pancreas, stomach, small intestine, large
20 intestine, brain, muscle and bone matter) were detached and weighed. The main
21 organs were finally rinsed with buffer and the remaining cell-associated radioactivity
22 was measured with a γ-counter.,

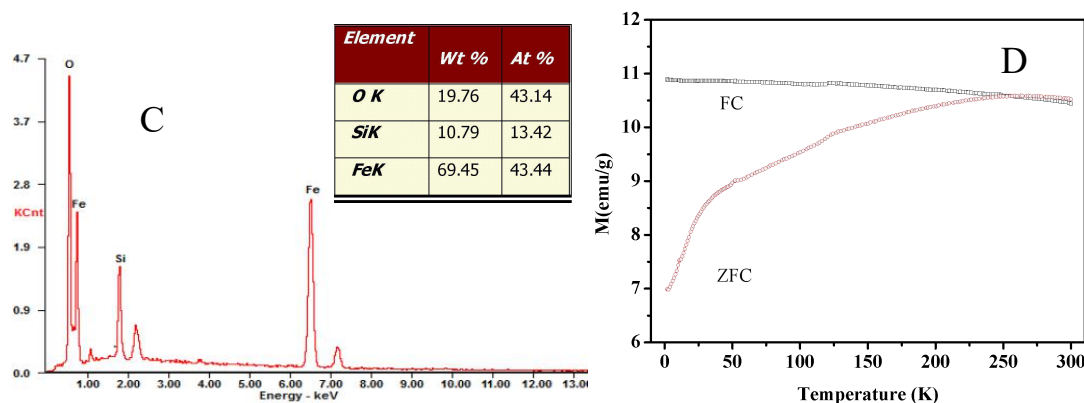
23 **3. Results and Discussion**

24 3.1 Characterization of Fe(0)@SiO₂



1

2



3

4

5

Fig. 3. (A)XRD pattern, (B) IR Spectra, (C) EDS images and (D) the ZFC-FC curve of Fe(0)@SiO₂

6 Fig. 3A(a) showed the broad diffraction peak occurring around $2\theta=24^\circ$ should be
 7 the characteristic diffraction peak of the amorphous SiO₂. The obvious diffraction
 8 peak appearing at $2\theta=45^\circ$ might be the characteristic diffraction peak of (211)
 9 ($2\theta=45.15^\circ$) or the (110) ($2\theta=44.94^\circ$) crystal plane of Fe(0). The Fe phase might
 10 occur in the product due to the strong reducing property of NaBH₄, which reduced
 11 Fe³⁺ to iron metal. Many experiments used NaBH₄ to reduce metals or metal alloys. In
 12 addition, in the XRD pattern of the product, no obvious diffraction peaks appeared at
 13 $2\theta=34.5^\circ$ and $2\theta=47^\circ$ or 49° , indicating that there was no other phase in the product,
 14 proving that the synthesized product is Fe(0).

1 The magnetic nano-spheres Fe(0)@SiO₂ was characterized by IR (Fig. 3B). The
2 strong absorption peak of 1087.8 cm⁻¹ in the infrared map was the characteristic
3 absorption peak of the Si-O bonds. It showed that the synthesized product has silica,
4 and the product should be Fe(0)@SiO₂, which is consistent with the XRD analysis
5 results.

6 As can be observed from the EDS analysis results recorded in Fig. 3C, The main
7 elements in the product were Si, Fe and O, which may be caused by the direct
8 reduction of part of Fe³⁺ to Fe(0) due to the strong reducibility of NaBH₄ in the
9 preparation of Fe(0)@SiO₂, resulting in the increase of the atomic number ratio of Fe.
10 The number of atoms of O and Si was much larger than 2, which is the proportion of
11 O element of OH on the surface of the material increasing the ratio of O.

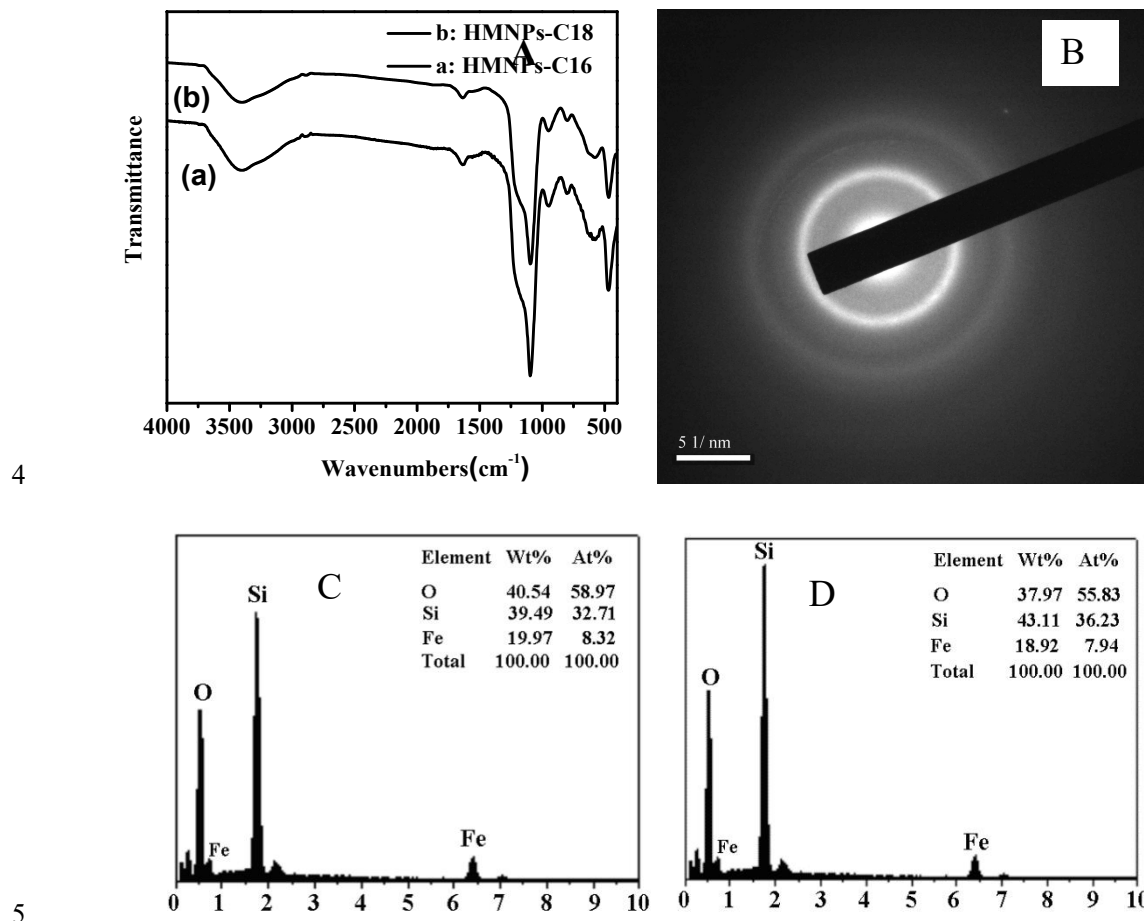
12 The zero field cooling and field cooling curves of Fe(0)@SiO₂ was shown by Fig.
13 3D. As the ZFC curve was quite different from the FC curve of Fe(0)@SiO₂, We
14 could know that Fe(0)@SiO₂ has superparamagnetism and magnetization of the
15 material is mainly affected by the external magnetic field.

16 3.2 Characterization of hollow magnetic nano-spheres HMFe-Si-C_n

17 The hollow magnetic nano-spheres HMFe-Si-C₁₆ and HMFe-Si-C₁₈ were
18 characterized by IR respectively (Fig. 4A). The asymmetric stretching and symmetric
19 stretching of Si-O-Si were exhibited at 1090.2 cm⁻¹, 796 cm⁻¹ and 467.1 cm⁻¹,
20 respectively. In addition, the stretching vibrations of Si-OH groups at 957.5 cm⁻¹
21 illustrated that higher surface area was occurred[23]. The stretching band at 1634 cm⁻¹
22 may be attributed to the presence of residual physisorbed water molecules.

23 As can be observed from the EDS analysis results recorded in Fig. 4(B, C), both
24 HMNPs-C₁₆ and HMNPs-C₁₈ only contain three elements Si, Fe and O, whose
25 corresponding atomic ratios are 3.9:1:7 and 4.6:1:7 respectively, greater than that

1 typical observed 1 : 2 for Si : O ratio in SiO₂, this is owing to the fact that the
 2 oxygen atoms in SiO₂ are able to coordinate to the Fe atoms, in which the Si atom and
 3 the Fe atom share an oxygen atom to form a complex.



6 Fig. 4. (A) SAED of HMFe-Si-C₁₆, IR Spectra, (B) (C) and (D) EDS images of HMFe-Si-C₁₆
 7 and HMFe-Si-C₁₈;

8 In the selection of electron diffraction (SAED) patterns, halo patterns were
 9 observed, as seen in Fig. 4B. Weak diffraction spots were formed corresponding to
 10 the first halo-diffraction ring in SAED. These diffuse spots were considered from
 11 coherently scattered electrons, and the scattered spots were from the disordered matrix
 12 atoms, and perhaps attributed to vague lattice in the Fe.

13 3.3 Transmission electron microscopy (TEM) analysis

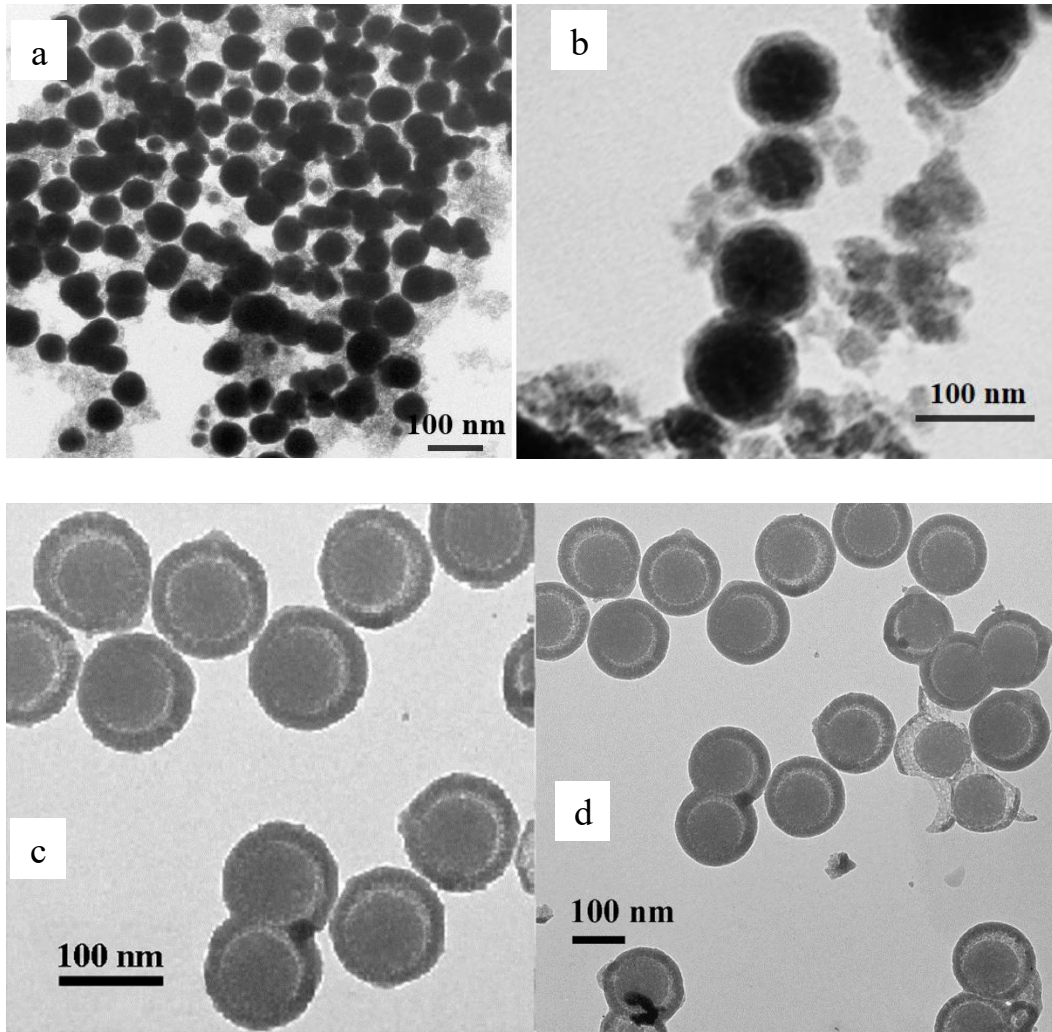


Fig.5. TEM images of (a), (b) Fe(0)@SiO₂, (c) HMFe-Si-C₁₆, and (d) HMFe-Si-C₁₈

The Fe(0)@SiO₂ nanoparticles synthesized by aqueous phase one-pot method are spherical (Fig. 5a,b). According to Fig. 5a, the obtained Fe(0)@SiO₂ NPs have good dispersion and uniform particle size. When zoomed in, the microscopic structure of Fe(0)@SiO₂ NPs can be observed (Fig. 5b). The average particle size measured by electronic scale is about 60 nm, with acceptable dispersion and clear boundaries. Besides, Fe(0)@SiO₂ has apparent core-shell structure with a Fe(0) core around 60 nm and the SiO₂ coating of about 8.5 nm.

HMFe-Si-C₁₆ and HMFe-Si-C₁₈ are hollow spherical, have good dispersibility, and uniform particle size (Fig. 5c and Fig. 5d). The diameter of HMFe-Si-C₁₆ is about

1 117 nm. The core of Fe had a thickness of near 70 nm and the cavity thickness about
2 18 nm and silica shell having a thickness of 15 nm were clearly observed. The
3 diameter of HMFe-Si-C₁₈ is 156 nm. It was clearly observed that the core of Fe had a
4 thickness around 90 nm, a cavity thickness of 20 nm, and a silica shell thickness of
5 20.7 nm.

6 3.4 Scanning electron microscopy (SEM) analysis and particle size measurement by 7 laser-diffraction-size analyzer

8 To further observe the surface features of the synthesized products, the effects of
9 different chain lengths on the size of hollow magnetic nano-spheres were viewed by
10 scanning electron microscopy (SEM) methods. It can be observed from Fig. 6 that,
11 both HMFe-Si-C₁₆ and HMFe-Si-C₁₈ products all exhibit uniform particle size with
12 good dispersion. HMFe-Si-C₁₆ indeed consists of a number of spherical particles from
13 approximately 100 to 120 nm in diameter, less than that of HMFe-Si-C₁₈. As a
14 contrast, HMFe-Si-C₁₈ also clearly displays spherical particles in the diameter range
15 of 150~170 nm. The result of laser diffraction method also indicates the product of
16 HMFe-Si-C₁₆ has a rather narrow size distribution, the size distribution of the HMFe-
17 Si-C₁₆ centers around the range from 115.6 nm to 119.1 nm (Fig. 6). In a comparison
18 of HMFe-Si-C₁₆, the size distribution of the HMFe-Si-C₁₈ centers within the range of
19 152.0 nm to 162.8 nm. The results of size distribution are in agreement with the TEM
20 results.

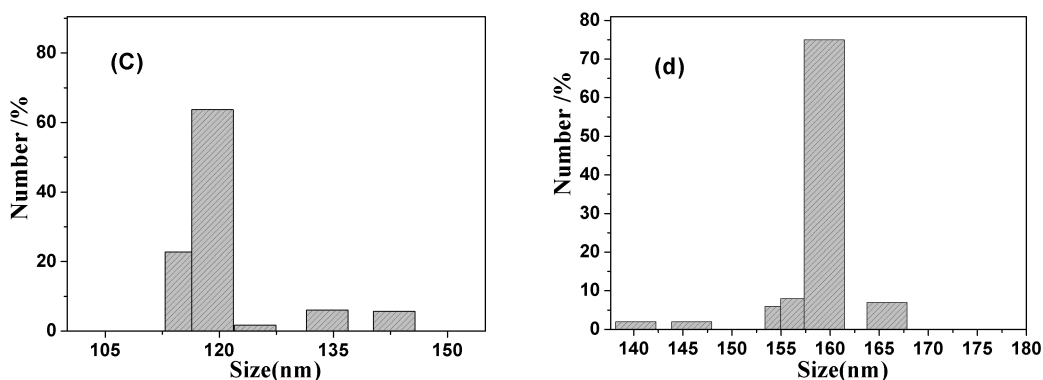
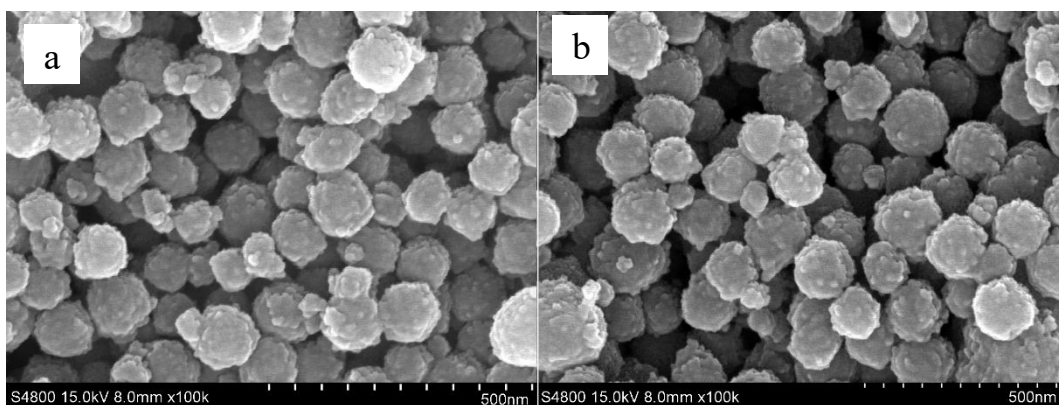


Fig. 6 SEM image of HMFe-Si-C₁₆ (a), HMFe-Si-C₁₈ (b) and HMFe-Si-C₁₆ (c), HMFe-Si-C₁₈ (d) nanoparticles size distribution

3.5 Mesoporous and magnetic properties of hollow magnetic nano-spheres

In order to study the drug (MMC) loading and release properties of hollow magnetic nano-spheres with different cavity structures, the ASAP2405N adsorption analyzer was used to determine nitrogen adsorption-desorption isotherms, from which the BET specific surface area was calculated by Brunauer-Emmett-Teller (BET) equation using the adsorption data in the relative pressure (p/p_0) range of 0.05~0.30. The pore volume and pore structure distribution of calcined HMFe-Si-C₁₆ and HMFe-Si-C₁₈ were obtained by the BJH method.

As can be seen from the nitrogen adsorption-desorption isotherms of HMFe-Si-C₁₆ and HMFe-Si-C₁₈ (Fig. 7A and B), both show the characteristics of the IV type isotherm in the IUPAC classification at the relative pressure of p/p_0 of 0.01~0.99,

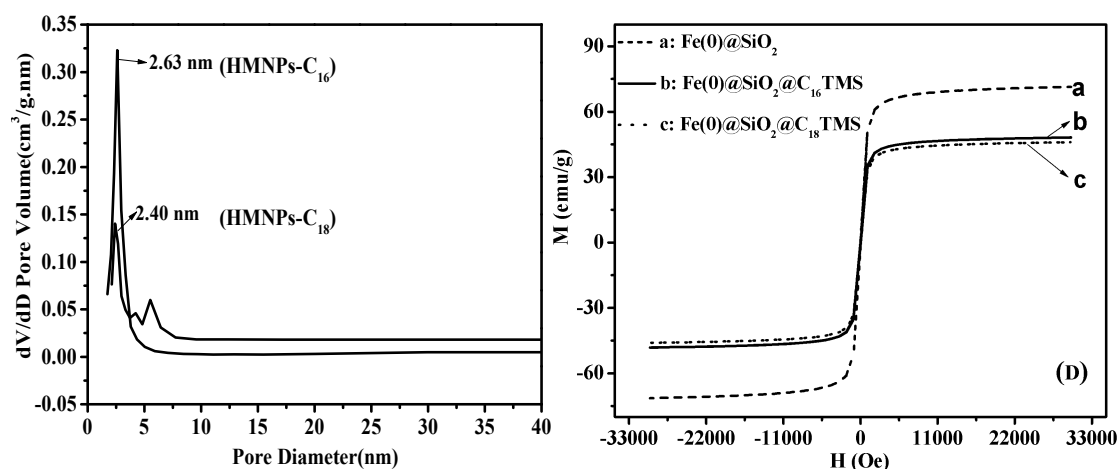
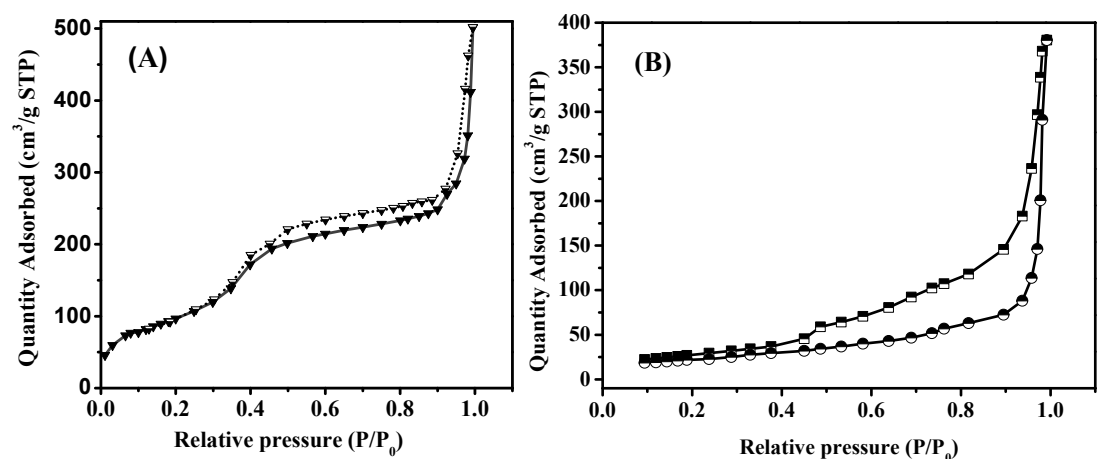
1 indicating the presence of mesopores. However, the adsorption isotherm of HMFe-Si-
2 C₁₆ has a distinction from that of HMFe-Si-C₁₈, the adsorption curve of the former is
3 convex upward at turning point of $p/p_0=0.3953$, demonstrating condensation of pores.
4 However, in contrast, the adsorption curve of the latter is concave upward at a turning
5 point of $p/p_0=0.8073$, demonstrating weak action between adsorbent and adsorbate
6 [24].

7 The physisorption isotherm of HMFe-Si-C₁₆ and HMFe-Si-C₁₈ all show
8 hysteresis loops. For the product of HMFe-Si-C₁₆, adsorption isotherm has mixed
9 types of H₂ and H₁ hysteresis loop [25], desorption is at first rapid at near saturation
10 but becomes much gradual at a relative pressure of about 0.9 (the “slope platform” of
11 the isotherm). The two branches in the slope platform of isotherm remain nearly
12 horizontal and parallel over a wide range of relative pressures between 0.45 and 0.9,
13 and the desorption boundary curve converges to the adsorption isotherm at a relative
14 pressure of about 0.45, indicating inkbottle type mesopores [26]. As reported by K
15 Morishige [27], a hysteresis loop of type H₂ and a steep desorption branch for HMFe-
16 Si-C₁₆ signifies disordered mesoporous materials.

17 In contrast, the adsorption isotherm of HMFe-Si-C₁₈ has a typical H₁ hysteresis
18 loop [28], and the two branches in the isotherm remain nearly vertical and parallel
19 between 0.80 and near saturation. The desorption boundary curve is not able to
20 converge to the adsorption isotherm from the beginning to end, demonstrating
21 cylindrical mesopores of uniform radius [28].

22 According to our previous work [20], the longer the surfactant chain lengths, the
23 higher ordered the products, which brings about differences of mesoporous properties
24 between HMFe-Si-C₁₆ and HMFe-Si-C₁₈. Accordingly, the longer dual-function
25 surfactant C₁₈TMS can generate more micelles, enhancing interaction between

1 silicates species and dual-function surfactant, thus favoring condensation of silicates
 2 species. As a template, the longer C₁₈TMS is able to direct the formation of HMFe-Si
 3 with higher ordered cylindrical mesopores and compact pore wall, while, in contrast,
 4 the shorter C₁₆TMS directs formation of HMFe-Si with disordered inkbottle type
 5 mesopores.



8
 9 Fig. 7. Mesoporous and magnetic properties of HMFe-Si, Low temperature N₂ adsorption-
 10 desorption isotherm curve of HMFe-Si-C₁₆(A) and HMFe-Si-C₁₈(B), pore size
 11 distribution of HMFe-Si(C) and magnetization curve of products (D)

12 Fig. 7(C) shows pore size distribution of HMFe-Si-C₁₆ and HMFe-Si-C₁₈. The
 13 most probable pore diameter of HMFe-Si-C₁₈ was 2.40 nm according to BJH (Barrett-
 14 Joyner-Halenda) desorption model. Nitrogen adsorption/desorption experiments

1 exhibited that the measured BET surface area was 106.19 m²/g, while the BJH pore
2 volume was 0.675 cm³/g. In comparison with the HMFe-Si-C₁₈; the product of
3 HMFe-Si-C₁₆ had a a little bigger size than that of HMFe-Si-C₁₈, this is because
4 capillary evaporation occurs via spontaneous cavitation of the condensed liquid in the
5 large cavities, when the cavity size is increased, the adsorption branch shifts into
6 higher relative pressures[29]. Its most probable pore diameter was 2.63 nm, with a
7 decrease in the BJH pore volume to 0.773 cm³/g, the calculated BET surface area
8 decreased to 383.52 m²/g accordingly.

9 The magnetic properties of the HMFe-Si-C₁₆ and HMFe-Si-C₁₈ were investigated
10 by a vibrating sample magnetometer (VSM BH-55) with fields up to 30 K Gauss at
11 room temperature. The product of Fe(0)@SiO₂ reduced in 4 vol% H₂ in N₂ at 400 °C
12 was also characterized by VSM. The M-H curves of products can be seen in Fig. 6(D).

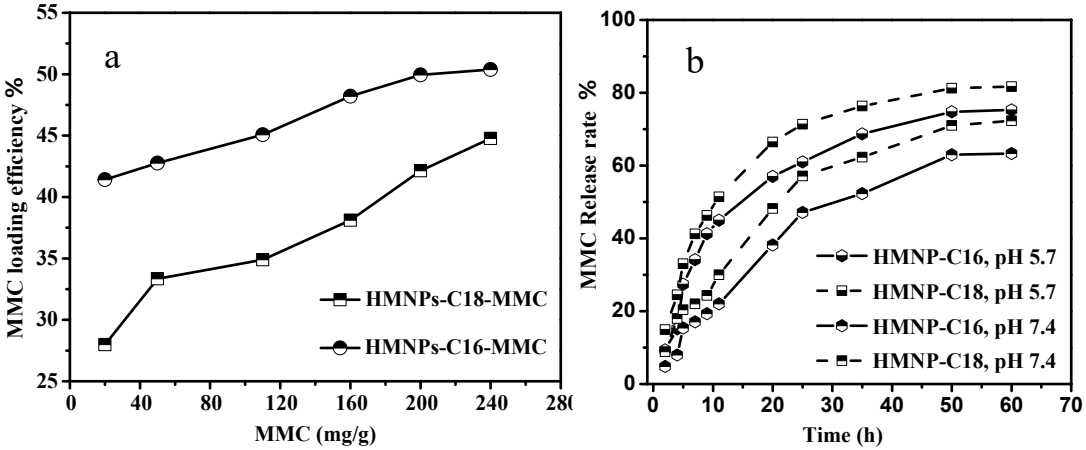
13 The M-H curves of the Fe(0)@SiO₂ after H₂ reduction display strong saturation
14 magnetization (Ms.) at 71.41 emu·g⁻¹ and with a minor residual magnetization of 1.45
15 emu/g, which can designate that the Fe(0)@SiO₂ was successfully obtained.

16 The Ms. value of hollow magnetic nano-spheres HMFe-Si-C₁₆ and HMFe-Si-C₁₈
17 were 50.01 emu·g⁻¹ and 45.30 emu·g⁻¹, respectively—both had a very minor residual
18 magnetization of about 0.65 emu·g⁻¹, and had a low coercivity around 28.60 Oe,
19 characteristics of good soft magnetic properties. Therefore, both were
20 easily collected by an external magnet, and gentle shaking could easily make them
21 well-dispersed throughout the solution.

22 The magnetic properties between HMFe-Si-C₁₆ and HMFe-Si-C₁₈ were compared.
23 The HMFe-Si-C₁₆ revealed a higher magnetization value than that of HMFe-Si-C₁₈;
24 owing to the fact that HMFe-Si-C₁₈ had a thicker silica shell (21.5 nm) than that of
25 HMFe-Si-C₁₆ (15 nm), a large shielding effect on magnetic properties of Fe(0) was

1 generated. In addition, based on the results of EDS analysis, a higher fraction of Fe
 2 atoms (8.32 %) in HMFe-Si-C₁₆ than that in HMFe-Si-C₁₈ (7.94 %) may lead to
 3 magnetic properties of HMFe-Si-C₁₆ being improved.

4 3.6 MMC loading efficiency and in vitro MMC release of HMFe-Si-C_n loaded MMC



5
 6 Fig. 8 MMC adsorption curve of HMFe-Si-C_n in 10 mM PBS (pH 7.4) and MMC release of
 7 HMFe-Si-C_n in 10 mM PBS (pH 5.7 and 7.4)

8 As shown in Fig. 8a, the amount of MMC adsorbed on both HMFe-Si-C₁₆ and
 9 HMFe-Si-C₁₈ increased with increasing initial concentration of MMC. When the
 10 initial MMC concentration attained 250 mg/g (1000 µg MMC/5 mg HMFe-Si), both
 11 adsorption curves were close to the saturated monolayer adsorption with the L shape
 12 of the curve exhibited, which revealed a type I curve for both adsorption curve in the
 13 BDDT classification, and was thus indicative of both open HMFe-Si-C₁₆ and HMFe-
 14 Si-C₁₈ framework with permanent microporosity. The findings are in agreement with
 15 the results shown in Fig. 7.

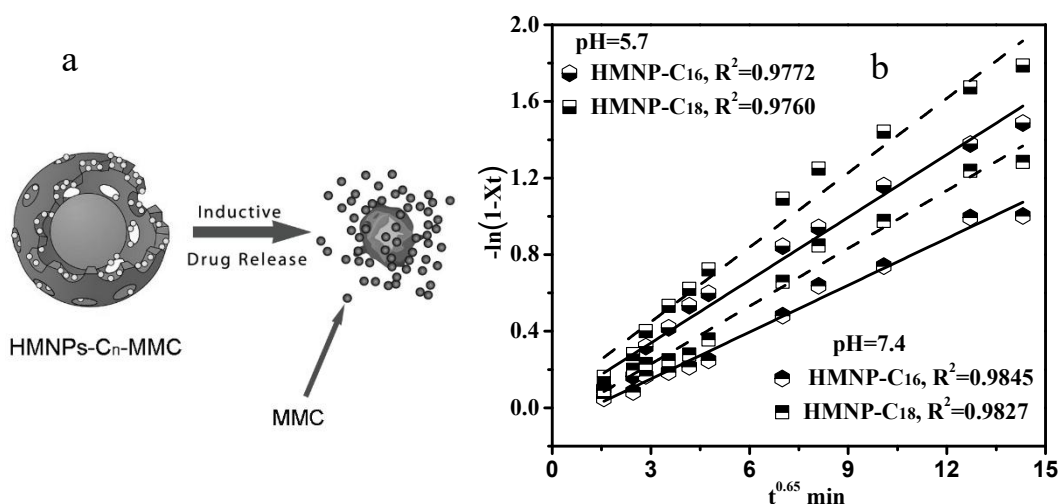
16 As shown in Fig. 8a, MMC loading efficiency of HMFe-Si-C₁₈ was lower than
 17 that of HMFe-Si-C₁₆ indicating the HMFe-Si-C₁₆ loaded larger amounts of MMC than
 18 that of the HMFe-Si-C₁₈. This is owing to the fact that the pore size, surface area, and
 19 pore volume of HMFe-Si-C₁₆ were larger than those of HMFe-Si-C₁₈.

20 The release rate of MMC on both HMFe-Si-C₁₆ and HMFe-Si-C₁₈ at different pH

1 levels (pH 5.7 and 7.4) is shown in Fig. 8b. It can be observed that the MMC release
 2 rate gradually increased within the first 20 h, with the release rate reaching
 3 equilibrium after 50 h. Both HMFe-Si-C₁₆ and HMFe-Si-C₁₈ all showed a clear pH-
 4 dependent drug release behavior; the release rate of HMFe-Si-C₁₆-MMC and HMFe-
 5 Si-C₁₈-MMC drug was relatively slow at pH 7.4, and slowed down after 7 h with an
 6 initial release of about 17 % and 22 %, respectively. After 50 h, their equilibrium
 7 release reached 63 % and 72 % for HMFe-Si-C₁₆-MMC and HMFe-Si-C₁₈-MMC,
 8 respectively.

9 In contrast, the release of the two hollow nano-spheres in 10 mM PBS solutions
 10 at a pH level of 5.7 was much faster, and also approximately 75 % and 81 % of the
 11 drug was released in the 10 mM PBS solution at a pH level of 5.7 for HMFe-Si-C₁₆-
 12 MMC and HMFe-Si-C₁₈-MMC drug, respectively, after 50 h. Drugs and hollow nano-
 13 spheres carry a positive charge at a lower pH, providing the necessary exclusion
 14 between them. These factors are the main drivers of drug release in acidic
 15 environments.

16 3.7 Drug diffusion mechanism of HMFe-Si-C_n loaded MMC



17

18 Fig. 9 Scheme (a) for release of MMC from HMFe-Si-C₁₆-MMC composites and (b) with $-\log(1-$

19 $X_t)$ as a function of $t^{0.65}$ in PBS solution (pH 7.4 and pH 5.7)

1 As can be seen from Fig. 9a, on account of their mesoporous SiO₂ thin shell and
2 a cavity of size about 65 nm, hollow magnetic nanoparticles act as a capsule for drug
3 molecule storage. MMC is uniformly loaded in the cavity of HMFe-Si-C_n; when the
4 MMC loaded HMFe-Si-C_n was dispersed in the normal 10 mM PBS solutions, both
5 adsorption and desorption took place in a reversible kinetic model.



7 As the MMC loaded HMFe-Si-C_n desorbed MMC into PBS solutions, the drug
8 release was unavoidably controllable in two stages attributable to relatively rapid
9 initial diffuse from outer surface adsorption, and slower permeation from inner void
10 through cavities. It is worth mentioning, that a residual amount of the drug remained
11 left within the cavity of HMFe-Si-C_n. This is owing to the fact that HMFe-Si-C_n
12 possessed circular voids and a mesoporous shell; having strong specific adsorption
13 ability to MMC molecules, it will take some time to reach the adsorption-desorption
14 equilibrium. An experiment was designed to verify this fact. Though the solution
15 remained clear before release of MMC, the solution changed to purple after the
16 release of MMC, fully demonstrating that the diffusion of MMC into PBS solutions
17 from MMC loaded HMFe-Si-C_n was spontaneous.

18 Once the MMC molecules diffuse through HMFe-Si-C_n hollow spheres, they
19 then diffuse through the diffusion layer. Thus the drug release could be controlled by
20 the diffusion through the HMFe-Si-C_n hollow spheres or by the diffusion through the
21 solution layer surrounding the hollow spheres. The release rate of drug molecules
22 would be determined by the slower step of these two processes. Bhaskar et al. [30]
23 developed a simple procedure to establish whether or not the diffusion through the
24 particle was the rate limiting step. For a particle diffusion-controlled release, Bhaskar
25 et al. [30] obtained the following equation:

$$\ln(1-X_t) = -1.59(6/d_p)^{1.3}D^{0.65}t^{0.65}$$

where d_p is particle diameter, and D is the diffusivity. This suggests that particle diffusion control can be tested by simply testing for linearity between $\log(1-X_t)$ and $t^{0.65}$. This method was applied to the experimental data, and a suitable linear relationship (correlation coefficient $R^2 \cong 0.9760$) was obtained for the pH 5.7 and 7.4 release respectively (see Fig. 8b), indicating that for these two pH releases, the diffusion through both HMFe-Si-C₁₆ and HMFe-Si-C₁₈ hollow spheres is the rate limiting step.

3.8 In vitro release kinetics of HMFe-Si loaded with MMC

According to L Xu [31], the slow release kinetics of HMFe-Si-C₁₈ and HMFe-Si-C₁₆ on MMC can be treated using pseudo-first-order and pseudo-second-order models.

The pseudo-first-order rate expression can be written as: $\log(Q_e - Q_t) = \log Q_e - \frac{k_1}{2.303}t$;

here, Q_t means the release amount of MMC (%) at time t (h), Q_e refers to the release amount of MMC when balancing (%), and k_1 is the release rate constant (1/h).

The pseudo-second-order model rate expression can be written as:

$$\frac{t}{Q_t} = \frac{1}{k_2 Q_e^2} + \frac{1}{Q_e}t$$

In the equation, k_2 refers to the release rate constant (1/h).

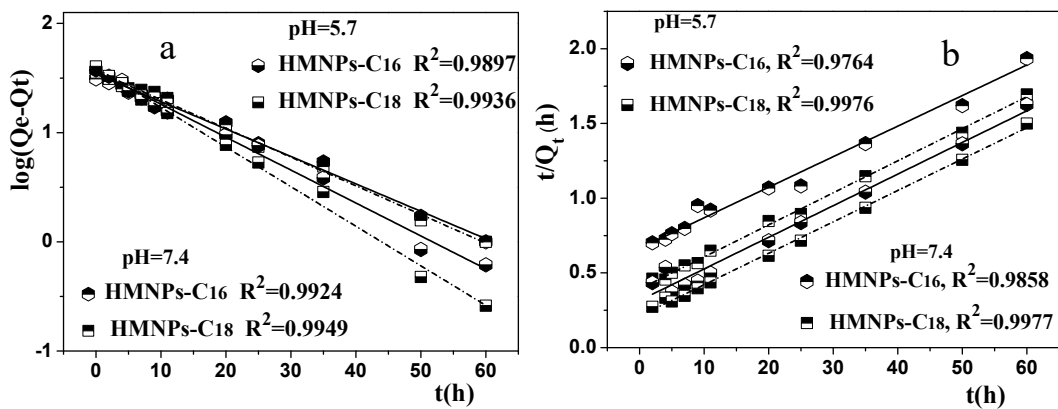


Fig. 10. Pseudo-first-order (a) and pseudo-second-order (b) of MMC release processes in the PBS

1 (pH 5.7 and 7.4) from both HMFe-Si-C₁₆ and HMFe-Si-C₁₈

2 With the simulation of the above two kinetic models for release kinetic data, it
3 was found that the pseudo-first-order is more satisfactory for describing the release
4 kinetic process of MMC from HMFe-Si-C₁₆-MMC composites than that of the
5 pseudo-second-order. Fig. 10a shows the plot of $\log(Q_e - Q_t)$ vs. t for the release of
6 MMC at pH 5.7 and 7.4 environments, respectively, and as can be seen, fair straight
7 lines were obtained. For the pH 5.7 release, the correlation coefficient (R^2) and k_1
8 values are 0.9897 and 0.06944 h⁻¹, respectively, and for the pH 7.4 release, they are
9 0.9924 and 0.05790 h⁻¹, respectively. The release kinetics result is not similar to the
10 HMFe-Si-C₁₈-MMC composites, for which, pseudo-second-order is more satisfactory.
11 Fig. 10b shows the plot of t/Q_t vs. t for the release of MMC at pH 5.7 and 7.4
12 environments, respectively, and as can be seen, fair straight lines were obtained. For
13 the pH 5.7 release, the correlation coefficient (R^2) and k_2 values are 0.9976 and
14 0.002093 h⁻¹, respectively, and for the pH 7.4 release, they are 0.9977 and 0.001173 h⁻¹,
15 respectively.

16 The difference between of HMFe-Si-C₁₆-MMC and HMFe-Si-C₁₈-MMC
17 composites in release kinetics results from the different pore structures of HMFe-Si-
18 C₁₆ and HMFe-Si-C₁₈. In the adsorption-desorption equilibrium, the surface charge of
19 sorbents and hydrogen bonding between the groups of MMC and the silanol groups
20 packed on the pore wall may be the chief force to hold MMC molecules in HMFe-Si-
21 C_n hollow spheres. The interaction between two materials and MMC molecules is
22 different, resulting in different release kinetics [31].

23 In contrast to HMFe-Si-C₁₆, the faster release of HMFe-Si-C₁₈ was actually
24 related to the weaker interaction with MMC molecules. HMFe-Si-C₁₆ has disordered
25 inkbottle type mesopores with an open pore diameter of about 2.63 nm. When HMFe-

1 Si-C₁₆ was used as a vehicle to encapsulate the MMC drug, the drug was not arranged
 2 in a crystalline form on account of space confinement [32]. When confined to the
 3 narrow pores, and disordered inkbottle pore space, MMC molecules were prevented
 4 from arranging themselves into a crystal lattice. Consequently, once release of MMC
 5 out of the inkbottle pore space occurs, it may take a “vacancy” state, which is
 6 consistent with the pseudo-first-order model. Fig. 8b exhibits that, no matter what pH
 7 condition, HMFe-Si-C₁₆-MMC composites have lower release percentages of MMC
 8 in the first 30 min, implying that the disordered inkbottle pore space of HMFe-Si-C₁₆
 9 can prevent leaching of the loaded MMC molecules before the HMFe-Si-C₁₆-MMC
 10 were taken up by cells. This is another advantage of using HMFe-Si-C₁₆ as drug
 11 vehicles for intracellular drug delivery applications. In current work, HMFe-Si-C₁₆
 12 was considered to be an optimum preparatory radioactively labeled vehicle.

13 3.9 Labeling efficiency and Technetium-99m (^{99m}Tc^m) labeled HMFe-Si-C_n

14 Table 1 Our data for ^{99m}Tc-labelled HMFe-Si-C_n

Stay ^{99m} Tc- labelled	Initial activity of Na ^{99m} Tc ^m O ₄	Syringe's residual activity	Activity in wash fluids, clear liquor	^{99m} Tc-labelled HMFe-Si	Labeling efficiency
HMFe-Si- C ₁₆	4.90 mCi	0.28 mCi	2.70mCi	1.30 mCi	30.4%
HMFe-Si- C ₁₈	4.90 mCi	0.28 mCi	2.65mCi	1.35mCi	31.5 %

15

16 From Table 1, the labeling efficiency of magnetic hollow spheres HMFe-Si-C₁₈
 17 and HMFe-Si-C₁₆ were calculated as 31.5% and 30.4% respectively; both considering
 18 4.90 mCi ^{99m}Tc^m decay to 4.28 mCi in the experiment. In comparison with the results
 19 of Zhang et al. [33] by complexation labeling of ^{99m}Tc^m with DTPAA, the current work
 20 exhibits low the labeling efficiency of ^{99m}Tc^m. This is ascribed to the fact that the issues

1 of $^{99}\text{Tc}^{\text{m}}$ labeled HMFe-Si-C_n were involved in both cavity physical adsorption and
2 the thermodynamic equilibrium. Therefore, it is necessary for $^{99}\text{Tc}^{\text{m}}$ labeled HMFe-Si-
3 C_n to reach the equilibrium for a long enough time. Once the equilibrium of physical
4 adsorption is reached, the $^{99}\text{Tc}^{\text{m}}$ labeled HMFe-Si-C_n reaches saturation, and so
5 HMFe-Si-C_n chose to no longer continue labelling additional $^{99}\text{Tc}^{\text{m}}$.

6 Table 1 shows that the $^{99}\text{Tc}^{\text{m}}$ -labeling efficiency of HMFe-Si-C_{18} is higher than
7 that of HMFe-Si-C_{16} ; Although the $^{99}\text{Tc}^{\text{m}}$ -labeling efficiency of magnetic hollow
8 spheres HMFe-Si-C_n is relatively low, the $^{99}\text{Tc}^{\text{m}}$ -labeling efficiency by physical
9 adsorption can completely achieve the radiation intensity required for in vivo
10 targeting of functional magnetic anticancer drug by using conventional isotopic tracer
11 method [34-35].

12 Employing $^{99}\text{Tc}^{\text{m}}$ labeled magnetic HMFe-Si-C_n is a novel, simple and
13 convenient route. For this reason, $^{99}\text{Tc}^{\text{m}}$ labeled HMFe-Si-C_n by physical adsorption
14 can immediately be delivered into ICR mice via tail vein injection to observe in vivo
15 targeting distribution of magnetic anticancer drug with the addition of magnetic
16 targeting. The route for complexation labeling of $^{99}\text{Tc}^{\text{m}}$ with DTPAA is a lengthy and
17 complicated method, requiring not only amino functionalization of magnetic hollow
18 spheres, but also mono-coupling with diethylenetriaminepentaacetic acid (DTPAA).
19 Therefore, $^{99}\text{Tc}^{\text{m}}$ labeled HMFe-Si-C_n by simple physical adsorption has the
20 advantages of convenient and rapid quantification and localization in vivo.

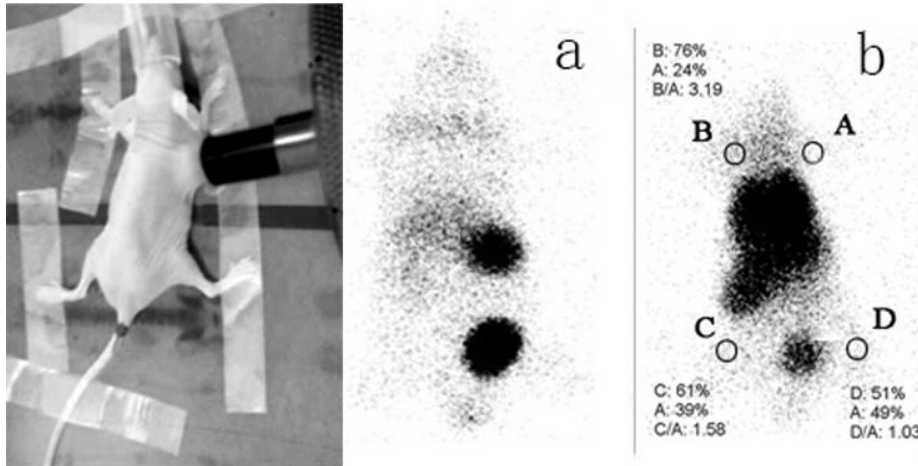
21 3.10 HMFe-Si-C_{16} targeting in vivo

22 Due to the wide distribution of each labelled hollow magnetic spheres
23 throughout the body after the injection of $\text{HMFe-Si-C}_{16}\text{-}^{99}\text{Tc}^{\text{m}}$, high levels of
24 radioactivity accumulation were observed in the liver, spleen, lung, and bladder after
25 2 h post injection, with a small amount of radioactive particles uptaking in the kidney

1 (Fig. 11 a). The results show that the $^{99}\text{Tc}^{\text{m}}$ labelled HMFe-Si-C₁₆ spheres can
2 successfully break through the pulmonary circulation, and can be excreted through the
3 urinary system. Instead, the HMFe-Si-C₁₆- $^{99}\text{Tc}^{\text{m}}$ spheres were swallowed by the
4 reticuloendothelial system (lung, liver and spleen).

5 In order to explore the targeting properties of $^{99}\text{Tc}^{\text{m}}$ labelled HMFe-Si-C₁₆- $^{99}\text{Tc}^{\text{m}}$
6 spheres, the tumors of nude mice were placed on the magnetic pole of the YMC-11
7 medical pulse magnetic field generator with the output voltage of pulsed magnetic
8 fields being controlled at 700 V for 2h. In the Fig. 11 b, the right forelimb (A) is
9 normal, the left forelimb (B) is the tumor region with targeting, the left hind limb (C)
10 is the tumor region with no targeting and the right hind limb (D) is a sense of
11 inflammation.

12 Fig. 11b shows nude mice SPECT imaging targeting for limb after injection. The
13 intensive distribution of black dots in the image correspond to the large amount of
14 $^{99}\text{Tc}^{\text{m}}$ labelled HMFe-Si-C₁₆- $^{99}\text{Tc}^{\text{m}}$ spheres that were accumulated into the tumor sites
15 by a combination of passive magnetic targeting and active targeting mechanisms. In
16 comparison with in vivo bio-distribution of $^{99}\text{Tc}^{\text{m}}$ labelled HMFe-Si-C₁₆ spheres, the
17 targeting SPECT imaging showed the activity concentration of $^{99}\text{Tc}^{\text{m}}$ labelled HMFe-
18 Si-C₁₆ spheres in the tumors were significantly higher than that without targeting, the
19 experimental data of $B_{\text{tumor targeting}}/A_{\text{normal}}$ at 3.19 and $C_{\text{tumor no targeting}}/A_{\text{normal}}$ at 1.58
20 demonstrated these facts. In addition, the experimental data of $C_{\text{tumor no targeting}}/A_{\text{normal}}$ at
21 1.58 demonstrated that $^{99}\text{Tc}^{\text{m}}$ labelled HMFe-Si-C₁₆ spheres tended to accumulate in
22 the tumor sites in vivo, implying $^{99}\text{Tc}^{\text{m}}$ labelled HMFe-Si-C₁₆ spheres have a good
23 affinity to the tumor.



1
2 Fig. 11 The SPECT images of the mouse after injection with HMFe-Si-C₁₆-^{99m}Tc spheres by (a)
3 no targeting and (b) targeting.

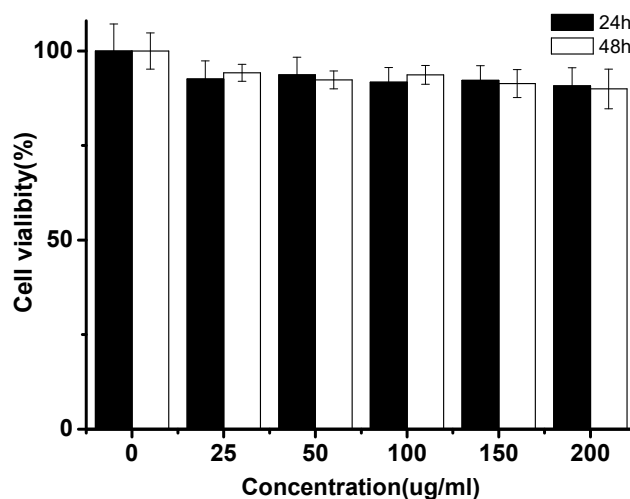
4 Table 2 shows the results of magnetically targeted radiotherapy employed ^{99m}Tc^m
5 labelled HMFe-Si-C₁₆ spheres. The liver uptake of ^{99m}Tc^m labelled HMFe-Si-C₁₆
6 spheres was 14.6915, 19.2382, 28.9201, 38.0013 and 35.6282% ID/g at 15, 30, 60,
7 120 and 180 min respectively. The radioactivity in the spleen was 33.2598, 43.5203,
8 89.0264, 121.0420 and 69.2384% ID/g at 15, 30, 60, 120 and 180 min, respectively.
9 The results showed HMFe-Si-C₁₆ had the highest spleen uptake of ^{99m}Tc^m for 180 min
10 after the injection; when the absolute organ uptake was compared, uptake by the lung
11 was the second highest, and uptake by the liver was the third highest. The findings
12 were in agreement with SPECT imaging data with high levels of ^{99m}Tc^m labelled
13 HMFe-Si-C₁₆ spheres uptake in the liver, spleen and lung. Furthermore, 4.7836 % of
14 radioactive particle uptake was found in the bone for 180 min after the injection,
15 indicating the ^{99m}Tc^m labelled HMFe-Si-C₁₆ spheres were able to gradually accumulate
16 in the bone with the lapse of time. On the contrary, relatively low radioactivity uptake
17 was observed in the pancreas, brain, and muscle. This is likely because ^{99m}Tc^m labelled
18 HMFe-Si-C₁₆ spheres were rapidly cleared by the pancreas, brain, and muscle, and
19 excreted by the mouse through the urine.

20 Table. 2 Biodistribution of ^{99m}Tc^m labelled HMFe-Si-C₁₆ spheres in mice (% ID/g)

tissues	15 min	30 min	60 min	120 min	180 min
blood	1.5902	1.2601	1.4781	2.9036	2.1559
heart	1.4823	1.4601	2.5705	2.0721	1.6591
lung	54.0404	54.5706	67.6554	60.4534	60.3154
kidney	3.2623	4.2060	5.9933	10.3055	9.9447
liver	14.6915	19.2382	28.9201	38.0013	35.6282
spleen	33.2598	43.5203	89.0264	121.0420	69.2384
pancreas	0.4632	0.6518	0.7561	0.9074	0.7151
stomach	1.0481	1.3038	2.4930	2.4035	2.4406
small intestine	1.0231	1.1407	1.5061	1.9020	1.4596
large intestine	0.6202	0.8649	1.2040	1.6369	1.5288
brain	0.0609	0.0504	0.0776	0.1105	0.1240
muscle	0.2601	0.3416	0.3484	0.4480	0.4244
bone	1.6718	2.2664	3.8863	5.3645	4.7836

1

2 3.11 In vitro cytotoxicity against HeLa cells of HMFe-Si-C₁₆ spheres



3

4 Fig. 11 Cell viabilities of HeLa cells after incubation with different concentrations of HMFe-Si-
5 C₁₆ spheres for 24 and 48 h.

6 The in vitro cytotoxicity against HeLa cells was investigated to evaluate the
7 potential application for HMFe-Si-C₁₆ spheres as a drug carrier (Fig.11). HMFe-Si-

1 C₁₆ spheres were selected as the model, and the results show that a 24 h and 48 h
2 incubation of HeLa cells with different concentrations of sample with 0, 25, 50, 100,
3 150, and 200 $\mu\text{g mL}^{-1}$. The results indicate that HMFe-Si-C₁₆ spheres show no
4 cytotoxicity to the HeLa cells with different concentrations. Even though the
5 concentration of sample reached up to 200 $\mu\text{g mL}^{-1}$, the surviving fraction of HeLa
6 cells is still up to 91 % for 24 h and 90 % for 48 h, indicating that HMFe-Si-C₁₆
7 spheres have relatively good biocompatibility.

8 **4. Conclusion**

9 In summary, the hollow magnetic nano-spheres of both HMFe-Si-C₁₆ and
10 HMFe-Si-C₁₈ were synthesized and directed by dual-function template. The long
11 alkyl chain n-octadecyl Trimethoxysilane directed assembly of HMFe-Si-C₁₈ with the
12 size of 160 nm, and the short alkyl chain n-hexadecyl Trimethoxysilane directed
13 assembly of HMFe-Si-C₁₆ with the size of 119 nm, demonstrating our proposed
14 synthesis strategy. On account of large surface area and pore volume, HMFe-Si-C₁₆
15 has higher MMC loading efficiency. A good linearity between $\log(1-X_t)$ and $t^{0.65}$ was
16 found for both HMFe-Si-C₁₆ and HMFe-Si-C₁₈, demonstrating the diffusion through
17 hollow magnetic nano-spheres was the rate limiting step. MMC drugs can be
18 efficiently loaded into the hollow magnetic nano-spheres HMFe-Si-C_n, and be
19 released through acid-assisted diffusion/dissolution controlled kinetics. Release
20 kinetics of the HMFe-Si-C₁₈-MMC was well described by pseudo-second-order
21 equation, but pseudo-first-order was more satisfactory for release kinetics of HMFe-
22 Si-C₁₆-MMC. This is owing to the fact that HMFe-Si-C₁₈ had ordered cylindrical
23 mesopores, while HMFe-Si-C₁₆ had disordered inkbottle pores, which could
24 potentially prevent leaching of the loaded MMC molecules before they were taken up
25 by cells. Accordingly, as an optimum vehicle, HMFe-Si-C₁₆ hollow spheres exhibited

1 a relatively high saturation magnetization ($50.01 \text{ emu}\cdot\text{g}^{-1}$) and could be labeled with
2 radioisotope $^{99}\text{Tc}^{\text{m}}$. This allowed $^{99}\text{Tc}^{\text{m}}$ labelled HMFe-Si-C₁₆ to be injected into the
3 mice to study the biodistribution of magnetic nanoparticles in different organs, and
4 the results, as well as MTT assays, revealed that HMFe-Si-C₁₆ spheres have relatively
5 acceptable biocompatibility, and were found to accumulate in the spleen, lung, liver,
6 and bone matter, showing obvious magnetic targeting effects.

7 **Acknowledgements** This work was supported by the National Natural Science
8 Foundation of China (20577010, 20971043), the Fundamental Research Funds for the
9 Central Universities, and the Open Project Program of State Key Laboratory of
10 Inorganic Synthesis and Preparative Chemistry, Jilin University.

11 **Declarations**

12 **Conflict interest** The authors have no relevant financial or non-financial interests to
13 disclose.

14 **Authors' contribution statement**

15 **Ziling Chang:** Methodology, Software, Investigation, Validation. **Yuxiang**
16 **Yang:** Conceptualization, Writing – original draft, Writing – review & editing
17 Supervision, Writing – review & editing, Funding acquisition. **Huafei Li:**
18 bioexperiment. **Hongming Yuan:** Conceptualization, Methodology, Writing – review
19 & editing. **Chaoying Ni:** Supervision, Writing – review & editing.

20 **References**

- 21 [1] M. Sastry, R. Fiala, R. Lipman, M. Tomasz, D.J. Patel, Solution Structure of the Monoalkylated Mitomycin C–
22 DNA Complex. *J. Mol. Biol.* **247**, 247-338 (1995)
- 23 [2] A.C. Sartorelli, W.F. Hodnick, M.F. Belcourt, M.Tomasz, B. Haffty, J.J. Fischer, S. Rockwell, Mitomycin C:
24 A Prototype Bioreductive Agent. *Oncol. Res.* **6**, 501-508 (1994)
- 25 [3] M. Önoł, Z. Aktaş, B. Hasanreisöđlu, Enhancement of the success rate in trabeculectomy: large - area
26 mitomycin-C application. *Clin. Experiment. Ophthalmol.* **36**(4), 316-322 (2008)

- 1 [4] Y. Zhu, W.G. Lu, L.Y. Zou, J.F. Feng, Magnetic Nanoparticles of Mitomycin C I. Preparation and Quality
2 Evaluation. *Chin. J. Pharm.* **37**(3), 168-171 (2006)
- 3 [5] M.E. Sharifabad, T. Mercer, T. Sen, The fabrication and characterization of stable core-shell
4 superparamagnetic nanocomposites for potential application in drug delivery. *J. Appl. Phys.* **117**(17),17D139
5 (2015)
- 6 [6] L.Yuan, X.R. Qi, Preparation and in vitro characterization of ATRA loaded mPEG-PLA diblock copolymeric
7 micelles. *Chin. J. New Drugs* **17**(3) 217-224, 227 (2008)
- 8 [7] N.K. Mal, M. Fujiwara, Y. Tanaka, Photocontrolled reversible release of guest molecules from coumarin-
9 modified mesoporous silica. *Nature* **421**, 350-353 (2003)
- 10 [8] V.-R.María, B. Francisco, A. Daniel, Mesoporous materials for drug delivery. *Angew. Chem. Int. Ed.* **46**(40)
11 7548–7558 (2007)
- 12 [9] I. I. Slowing, J. L. Vivero-Escoto, C.-W. Wu, and V. S-Y Lin, I. I. Slowing, J. L. Vivero-Escoto, C.-W. Wu,
13 and V. S-Y Lin. *Adv. Drug Deliv. Rev.* **60**(11), 1278 (2008).
- 14 [10] L. Zhang, T. Wang, L. Yang, C. Liu, C. Wang, H. Liu, Y.A. Wang, Z. Su, General route to multifunctional
15 uniform yolk/mesoporous silica shell nanocapsules: a platform for simultaneous cancer-targeted imaging and
16 magnetically guided drug delivery. *Chem. Eur. J.* **18**(39), 12512–12521 (2012)
- 17 [11] J. Liu, S.Z. Qiao, S.B. Hartono, G.Q. Lu, Monodisperse yolk-shell nanoparticles with a hierarchical porous
18 structure for delivery vehicles and nanoreactors. *Angew. Chem. Int. Ed.* **49**(29), 4981–4985 (2010)
- 19 [12] P.B. Santhosh, N.P. Ulrih, Multifunctional superparamagnetic iron oxide nanoparticles: promising tools in
20 cancer Theranostics. *Cancer Lett.* **336**(1), 8–17 (2013).
- 21 [13] M.M. Song, H. Bi, Y. Zhang, Fabrication of Fe@mSiO₂ nanowires with large remanence and low
22 cytotoxicity for targeted drug delivery[J]. *J. Appl. Phys.* **111**(7), 07B302 (2012)
- 23 [14] J. Yang, F. Zhang, Y. Chen, S. Qian, P. Hu, W. Li, Y. Deng, Y. Fang, L. Han, M. Luqman, D. Zhao, Core-
24 shell Ag@SiO₂@mSiO₂ mesoporous nanocarriers for metal-enhanced fluorescence. *Chem. Commun.* **47**, 11618-
25 11620 (2011)
- 26 [15] C. Wu, Z.Y. Lim, C. Zhou, W.G. Wang, S. Zhou, H. Yin, Y. Zhu, A soft-templated method to synthesize
27 sintering-resistant Au–mesoporous-silica core–shell nanocatalysts with sub-5 nm single-cores. *Chem. Commun.* **49**,
28 3215e-3217 (2013)

- 1 [16] T Ohhashi , T Tsuruoka, K Inoue, et al. An integrated function system using metal nanoparticle@ mesoporous
2 silica@ metal-organic framework hybrids[J]. *Microporous and Mesoporous Materials*, **245**, 04-108 (2017)
- 3 [17] T. Liu, Novel Hierarchically Structured Nanocomposites for Biomedical Applications[D]. Curtin University,
4 (2017)
- 5 [18] W. Zhao, H. Chen, Y. Li, L. Li, M. Lang, J. Shi, Uniform rattle-type hollow magnetic mesoporous spheres as
6 drug delivery carriers and their sustained-release property. *Adv. Funct. Mater.* **18**(18), 2780–2788 (2008)
- 7 [19] J. Zhang, C.Q. Lan, M. Post, B. Simard, Y. Deslandes, T.H. Hsieh, Design of Nanoparticles as Drug Carriers
8 for Cancer Therapy. *Cancer Genom. Proteom.* **3**(3-4),147–158 (2006)
- 9 [20] Y.X. Yang, H.P. Ying, J.G. Shao, A study on effect of different template chain length on synthesis of
10 mesoporous silica in acidic condition. *J. Am. Ceram. Soc.* **90**(11), 3460–3467 (2007)
- 11 [21] J.J. Yuan, X. Zhang, H. Qian, A novel approach to fabrication of superparamagnetite hollow silica/ magnetic
12 composite spheres. *J. Magn. Mag. Mater.* **322**(15), 2172-2176 (2010)
- 13 [22] S.Q. Shah, M.R. Khan & S.M. Ali, Radiosynthesis of $^{99m}\text{Tc}(\text{CO})_3\text{-Clinafloxacin}$ Dithiocarbamate and Its
14 Biological Evaluation as a Potential *Staphylococcus aureus* Infection Radiotracer. *Nucl. Med. Mol. Imaging* **45**,
15 248-254 (2011)
- 16 [23] Y. Chen, H. Chen, L. Guo, Q. He, F. Chen, J. Zhou, J. Feng, J. Shi, Hollow/rattle-type mesoporous
17 nanostructures by structural difference-based selective etching strategy. *ACS Nano.* **4**(1), 529–539 (2010)
- 18 [24] J.M. Yan, Q. Zhang, J.C. Gao, Adsorption and Coacervation. Beijing Science Press **115** (1986)
- 19 [25] K.S.W. Sing, R.T. Williams, Physisorption hysteresis loops and the characterization of nanoporous materials.
20 *Adsorpt. Sci. Technol.* **22**(10), 773-782 (2004)
- 21 [26] W.D. Xiang, Y.X. Yang, J.L. Zheng, Synthesis of mesoporous silica using cationic surfactant templating in
22 different inorganic acid source. *Mater. Science-Poland* **28**(3), 709-730 (2010)
- 23 [27] K. Morishige, M. Tateishi, F. Hirose, K. Aramaki, Change in desorption mechanism from pore blocking to
24 cavitation with temperature for nitrogen in ordered silica with cage-like pores. *Langmuir* **22**(22), 9220-9224 (2006)
- 25 [28] J.B. Zhang, Y.X. Yang, J.L. Zheng, Chin. Synthesis of Mesoporous Silica with a Three-Dimensional
26 Hexagonal Ordered Structure Using Cationic and Amphoteric Mixed Surfactants. *J. Inorg. Chemistry* **27**(9), 1817-
27 1829 (2011)

- 1 [29] K. Morishige, N. Tateishi, Adsorption hysteresis in ink-bottle pore. *J. Chem. Phys.* **119**(4), 2301-2306 (2003)
- 2 [30] R. Bhaskar, S.R.S. Murthy, B.D. Miglani, K.Viswanathan, Novel method to evaluate diffusion controlled
3 release of drug from resinate. *Int. J. Pharm.* **28**(1), 59–66 (1986)
- 4 [31] L. Xu, J. Dai, J. Pan, X. Li, P. Huo, Y. Yan, X. Zou, R. Zhang, Performance of rattle-type magnetic
5 mesoporous silica spheres in the adsorption of single and binary antibiotics. *Chem. Eng. J.* **174**, 221– 230 (2011)
- 6 [32] Y. Hua, Z. Zhi, Q. Zhao, C. Wu, P. Zhao, H. Jiang, T. Jiang, S. Wang, 3D cubic mesoporous silica
7 microsphere as a carrier for poorly soluble drug carvedilol. *Microporous Mesoporous Mater.* **147**(1), 94–101 (2012)
- 8 [33] J.X. Zhang, Q. Zhang, A.D. Huang, Determination of Biodistribution of Galactose
9 Polyhydroxyethylglutamine in Mice with Isotope ^{99m}Tc Labeling. *J. Instrum. Analysis* **22**(3), 69-71 (2003)
- 10 [34] M.C.F. Passos, C.F. Ramos, M. Bernardo-Filho, D.M.M. De Mattos, E. G. Moura, The Effect of Protein or
11 Energy Restriction on the Biodistribution of $\text{Na}^{99\text{m}}\text{TcO}_4$ in Wistar Rats. *Nucl. Med. Commun.* **21**(11), 1059-
12 1062 (2000)
- 13 [35] X. Xie, S. Deng, Comparative study on observing vascular crisis of rabbits with replanted limb by $\text{Na}^{99\text{m}}\text{TcO}_4$
14 trace imaging. *Nucl. Techniques* **11**, 011 (2005)